Space deployable parabolic reflector based on shape memory polymer composites

Guangqing Ming [a], Liwu Liu [b], Yanju Liu [b], Jinsong Leng [a],*

[a] Center for Composite Materials and Structures, Harbin Institute of Technology (HIT), P.O. BOX 3011, No.2 Yikuang Street, Harbin 150080, People's Republic of China
[b] Department of Astronautical Science and Mechanics, Harbin Institute of Technology (HIT), P.O. Box 301, No. 92 West Dazhi Street, Harbin 150001, People's Republic of China

ARTICLE INFO

ABSTRACT

In this paper, a deployable parabolic reflector based on epoxy-based shape memory polymer (SMP) is investigated. A deployable SMP composite parabolic reflector with a diameter of 400 mm is designed and fabricated according to laboratory equipment conditions. The storage ratio and collapsed surface curvature of the three folding patterns are compared using finite element analysis (FEA). Then FEA is used to analyze the reflector's folding and deploying process by investigating the shape memory behaviors during these two processes as well as predicting the deploying time. Finally, the reflector folding and deploying tests are completed. The reflector's shape fixation ratio, recovery ratio, and deploying time are measured to verify this pattern's feasibility and rationality.

1. Introduction

Shape memory polymers (SMPs) are a category of intelligent materials that can actively respond to external stimulation [1–3]. They have excellent strength and stiffness in their glassy state, while exhibiting good flexibility and outstanding large deformation capacity (up to 600 %) in their rubbery state. Based on the shape memory effect, after heating above the glass-transition temperature (T_g), it can be formed into a desired shape with considerable deformation, and then memorize this temporary shape as its temperature drops below T_g. When the temperature is above T_g again, it can recover its initial shape. Moreover, SMPs have the advantages of shock-free actuation, light weight and high performance in extreme environments. Hence, SMPs are applied in various fields, from aerospace to intelligent drives and biomedicine [4–9].

Space reflectors are widely applied in space telescopes, remote sensing cameras, space antennas, and other spacecraft equipment [10–15]. As the progress of space technology, the high resolution and high communication capability of this spaceflight equipment increases requirements for the aperture, surface precision, and light weight of the space reflectors [16–18]. In order to overcome the limitations of carrying capacity and space of rockets on large-scale and high-precision space reflectors, many countries such as the United States, Russia, and

Japan have developed deployable reflectors [19–21]. The most frequently developed type is a single deployable reflector. This reflector is built on the ground and folded. A rocket then launches it into a predetermined orbit, and it is ultimately deployed on-orbit by active or passive drive systems. These types of reflectors include solid surface, umbrella-like, truss, and semi-rigid deployable reflectors, etc. [22–26]. Among these, solid surface reflector is widely applied, and its advantages are high frequency, high data transmission rate, and high precision. However, most existing solid reflectors contain traditional mechanical structures. This reflector requires heavy and complex mechanical structures to ensure its folding and unfolding accuracy, while its mechanical mechanism and surface have different thermal expansion coefficients (CTE) that significantly affect its accuracy. Some deployable reflectors are designed to combine SMPs with flexible reflectors, which provide the advantages of high storage ratio, low surface density, and high frequency. This offers new ideas for developing deployable space reflectors.

The deployable parabolic reflector in this work was made of carbon fiber reinforced SMP composites. The geometric models for the folding state of the three folding patterns were obtained based on finite element simulation, the storage ratio and surface curvature of the folding state were compared, and a moderate "six petals" pattern was selected. Secondly, the viscoelastic constitutive theory of SMPs was used to simulate

* Corresponding author.
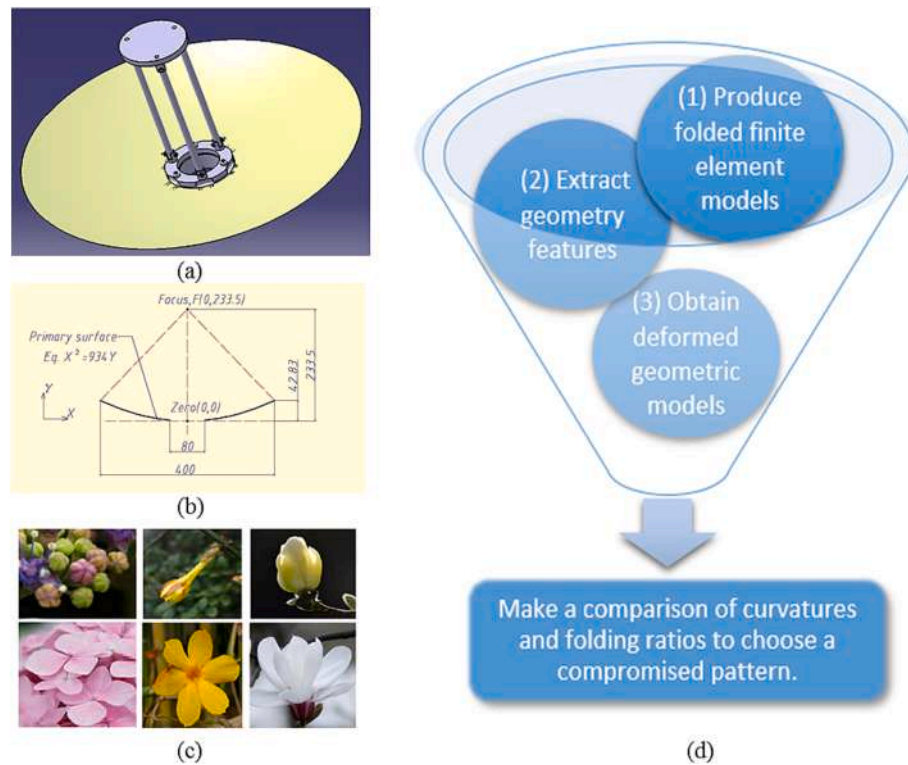*E-mail address:* lengjs@hit.edu.cn (J. Leng).

Fig. 1. (a) Model of the parabolic reflector; (b) Shape parameters of the reflector surface; (c) Different natural flowering patterns obtained from the internet; (d) Selection procedure of folding pattern.

the reflector's folding and deploying process in the commercial software ABAQUS. The energy and mechanical state of the shape memory behaviors were obtained from the simulation, as they are usually difficult to measure directly during experiments. Finally, the selected pattern was implemented to conduct folding and unfolding tests for the deployable reflector, while the reflector's shape fixation and recovery ratio were evaluated. The feasibility of the deployable parabolic reflector with SMP composites was verified, and the design experience for the further deployable reflectors was obtained.

2. Design

2.1. Surface type and folding pattern

Parabolic reflectors have superb reflectivity and high concentration, meeting high precision needs [27–29]. However, it is more difficult for the parabolic reflectors to fold, in contrast with other types of reflectors, such as cylindrical and planar reflectors. It is necessary to predict the surface curvature of the folded reflector and storage ratios for each pattern. Moreover, it is helpful to use finite element simulation analysis to forecast and make comparisons regarding these aspects.

The designed aperture of the lab-scale reflector is 400 mm. Its surface shape satisfies the parabolic equation $X^2 = 934Y$ (parabolic surface center as the origin of coordinates), shown in Fig. 1 (a) and (b). An 80 mm diameter reserved opening circle is in the reflector's middle. We intend to fold the reflector into a sound compact volume and feasible surface curvature just like a flower bud, as shown in Fig. 1 (c). However, it is important to determine the number of petals on the bud. In the next section, ABAQUS was implemented to produce finite element models for different folding patterns. Afterwards, geometry features can be extracted to obtain geometry models for analyzing and comparing different folding patterns. The selection procedure is shown in Fig. 1 (d).

2.2. Modeling and simulation

To obtain an optimal folding pattern with a reasonable storage ratio and folding curvature, three folding patterns for the deployable reflector were established in ABAQUS, as shown in Fig. 2 (a). Different numbers of rigid bars were used in different models, called the three-petal pattern, six-petal pattern, and nine-petal pattern respectively. Fig. 2 (b) shows three folding states for each reflector folding pattern. Then, geometry features such as edges and curved surfaces can be obtained from folded shapes of the finite element models to obtain geometric models. To easily observe the relative storage ratio and surface curvature, geometric models were placed together, as shown in Fig. 2 (c). Intuitively, the six-petal and nine-petal patterns are more efficient to store, and the three-petal pattern lacks a considerable storage ratio. Subsequently, the folding curvature and storage ratio will be quantitatively analyzed.

2.3. Folding patterns

2.3.1. Folding curvature

The folded state geometric models were imported into CATIA software for curvature analysis. Their maximum and minimum folding curvature can be obtained by using the visual window, as shown in Fig. 2 (d). Furthermore, the bottom 15 mm section along the height was omitted during curvature analysis because it involved unreasonable distortion derived from overly rigid boundary conditions that may affect evaluations of the pattern. Table 1 depicts the folding curvature for each pattern and compares them with the three-petal pattern, and the maximum curvature values for the other two increased by 43.48 % and 107.76 % respectively. And the curvature radius corresponding to the maximum curvature value can be calculated as about 31, 22, and 15 mm respectively.
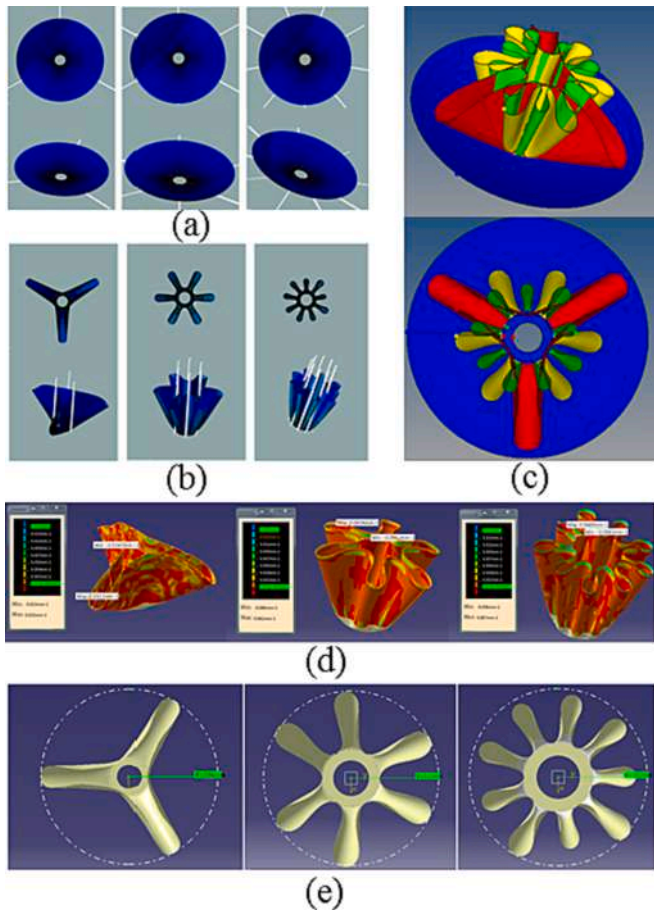
Fig. 2. (a) Finite element modeling of the three folding patterns from top view and axonometric view; (b) Finite element models of the three patterns after folding; (c) Comparison of geometric models of three folding patterns and original shape; (d) Surface curvature analysis of the three folding patterns; (e) Top view of the three folded pattern.

2.3.2. Storage ratio

The folded heights of the three patterns are consistent. Therefore, the circumcircle area (Fig. 2 (e)) of the folded reflector projection from the top view is able to approximately evaluate relative storage volume. Table 2 shows the folding aperture characterized by the circumscribed circle diameter. The decrement of the circumcircle area compared with the initial unfolding shape projection area is 13.51 %, 62.79 %, and 73.99 % respectively.

2.3.3. Discussion and results

In terms of folding curvature, the increment of the maximum curvature of the six-petal pattern compared with the three-petal pattern is just 43.48 %, but the increment of the nine-petal pattern increased sharply to 107.76 % (the curvature radius decreased to 15 mm). The remarkable increase in curvature negatively impacts the folding process by potentially damaging the reflector surface and resulting in an imprecise recovery shape. Meanwhile, a comparison of the folding apertures shows that the six-petal pattern has a compact folding volume (φ244 mm in folding aperture). Although the storage ratio of the nine-petal pattern has an increment, its decrement increases by only 11.2 %. Consequently, the six-petal pattern is more compromised. According to previous experimental experience, this pattern's folding curvature makes it feasible to fold the reflector, while the storage ratio is in an acceptable range. Therefore, the six-petal pattern was selected for further fabrication of shaping tools, analysis of shape memory behavior, and ground tests.

2.4. Folding and testing methods

To fold the reflector to the desired folded shape of the six-petal pattern, folding tools, shown in Fig. 3, were designed and fabricated. Six bars are uniformly distributed and hinged on the reflector base. Rotating the bars when the reflector is heated to above the glass transition temperature (T_g) can apply the folding forces to control the shaping of the folded reflector. To reduce stress concentration on the lower part during folding the reflector, we designed pairs of arcs on the mounting site. The schematic diagram of the folding and deploying tests is shown in Fig. 4, which will be described in detail in Section 5.Testing.

3. Materials and fabrication

Commercially available carbon fiber fabric (T300, 1 K, twill textile) and epoxy based SMP resin ($T_g = 100$ °C series) developed by Leng's group were used to fabricate a reflector utilizing Vacuum Assisted Resin Infusion (VARI) technology, a well-developed composite forming process. The reflector processing is shown in Fig. 5(a). Moreover, Fig. 5(b) shows the theory and detailed layers of the fabrication process, while Fig. 6 shows the manufacture and assembly process. Two layers of fabric with a [(0/90)/(±45)] stacking sequence were placed on the toughened glass mold, and then infused degassed SMP resin by applying vacuum negative pressure. This fabric then underwent the curing process (80 °C/3h → 100 °C/3h → 150 °C/5h) in an oven to yield the SMP composite reflector. The final reflector was trimmed of its redundant edge and mounted on the base, as shown in Fig. 6 (c).
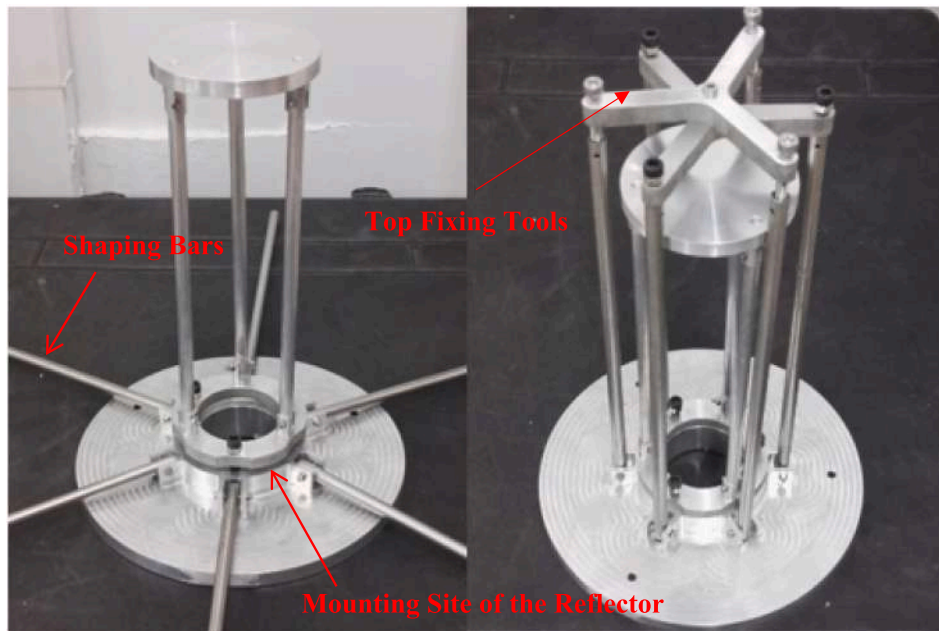
Table 1
Comparison of the folding curvature of the three folding patterns.

Folding patterns	Folding curvature Max (mm^{-1})	Folding curvature Min(mm^{-1})	MAX curvature MAX{|Max|,|Min|} (mm^{-1})	Increment(Compared with three-petal pattern)
Three-petal	0.0322	−0.0147	0.0322	0.00 %
Six-petal	0.0416	−0.0462	0.0462	43.48 %
Nine-petal	0.0669	−0.0581	0.0669	107.76 %

Table 2
Comparison of the folding aperture of the three folding patterns.

Folding patterns	Initial aperture (mm)	Folding aperture (circumscribed circle diameter) (mm)	Decrement of the area (compared with initial aperture)
Three-petal	φ400	φ372	13.51 %
Six-petal	φ400	φ244	62.79 %
Nine-petal	φ400	φ204	73.99 %

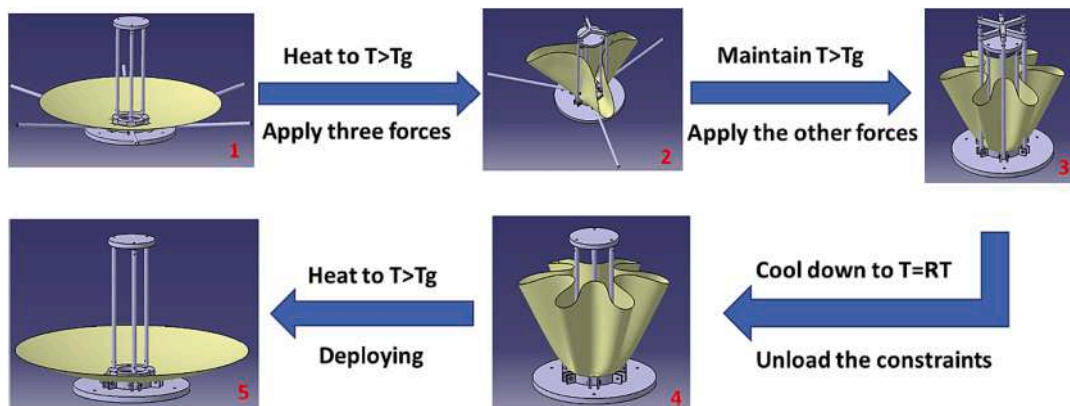**Fig. 3.** Folding tools of the deployable reflector.

Fig. 4. Schematic diagram of the folding and deploying process.

4. Simulation

4.1. Modeling of the reflector

The folding and deploying process was simulated using ABAQUS software based on the thermo-viscoelastic theory [30–33] using the Mooney-Rivlin (MR) hyper-elastic model and the generalized Maxwell model embedded in the ABAQUS software, the composites are treated as isotropic materials to simulate by homogenizing to simplify the simulation. The parameters used in the simulation are from Chen [34]. As shown in Fig. 7, the reflector finite element model was established using the linear four-node reduced integral shell element (S4R) that can prevent shear locking resulting from bending deformation. In addition, it has higher computational efficiency than complete integral because it decreases one point in each direction. As for meshing, the reduced integral element requires a finer mesh to overcome the hourglass problem, especially its large deformation and contact area. Hence, the reflector geometry model was divided into multiple regions to mesh. The reflector's areas that made contact with the deforming auxiliary bars were refined. Element quality control is shown in Table 3. The reflector center was fixed and six bars were coupled at six reference points that can rotate to control the reflector's folding in their own coordinate systems.

The simulation procedure settings are listed in Table 4. A total of five steps are set during the procedure. In Step 1, the temperature field is set to heat up from 30 °C to 120 °C. The six bars are set to rotate slightly (-0.1 rad) to make tender contact with the reflector to prevent non-convergence. Based on the contact during the last step, in Step 2, the reflector surface is shaped to a folded state by external force induced by −1.57 rad rotations of the six bars in the 120 °C temperature field. In Step 3, this surface cools down to 30 °C while maintaining its constraints for 180 s. In Step 4, this surface unloads its constraints. Step 1 to Step 4 demonstrates the overall folding process where the reflector is folded and fixed by itself. Step 5 simulates the process of shape recovery. The temperature increases from 30 °C to 120 °C within 100 s, enabling the reflector to successfully return to its initial shape.

4.2. Simulation results

Fig. 8 shows the process of folding using six bars to shape the reflector to its folded state. At 0 to 11 s (Fig. 8(a) to (b)), the deformation temperature field and pre-contact are implemented and ready to fold. At 11 to 21 s (Fig. 8(b) to (f)), 10 s in total, six bars are rotated to shape the reflector. The corresponding maximum stress is 1.77 MPa, 4.148 MPa, 6.887 MPa, and 13.83 MPa at 2 s, 4 s, 6 s, and 10 s of the shaping stage
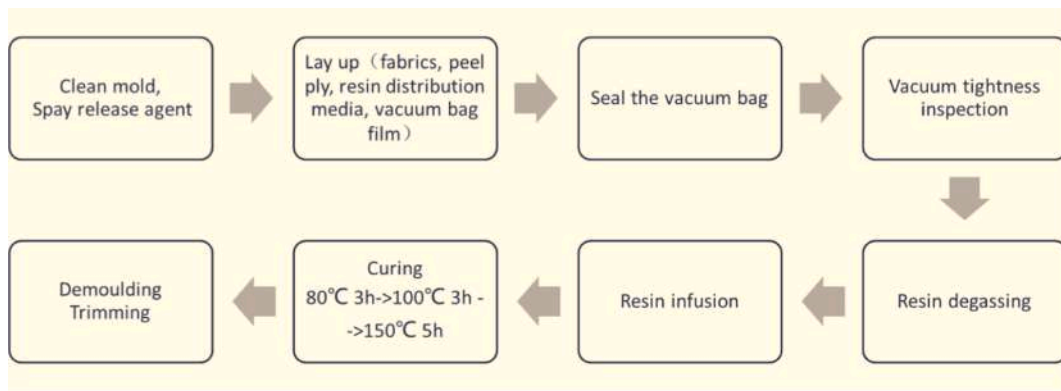
(a)
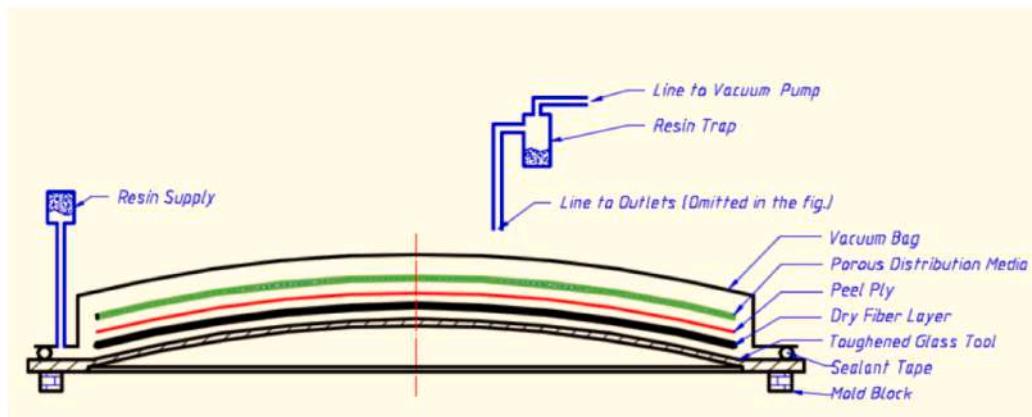
(b)

Fig. 5. (a) Process routing of the carbon fiber reinforced SMP composite reflector; (b) Schematic diagram of the layers during this process.

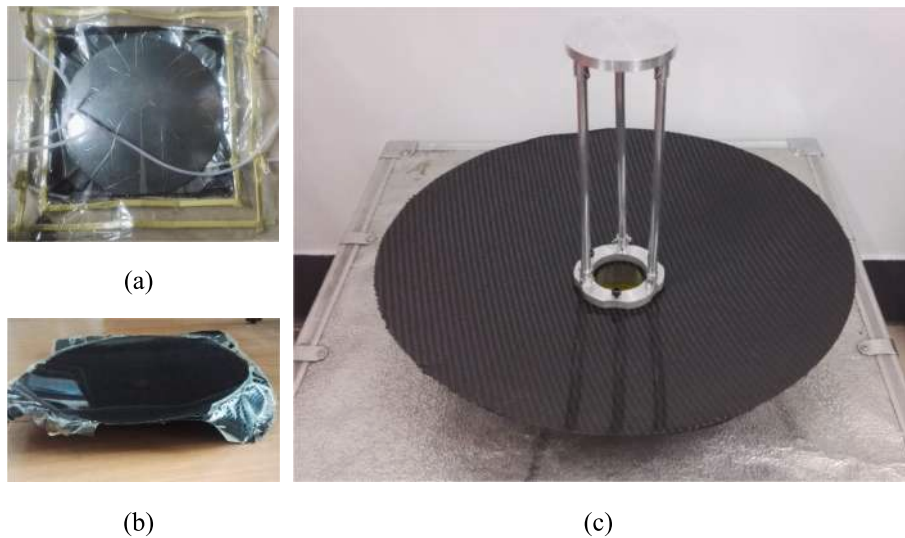

(a)

(b)   (c)

Fig. 6. (a) The reflector's fabrication process using VARI; (b) Reflector surface after demolding; (c) The deployable reflector after trimming and assembly.
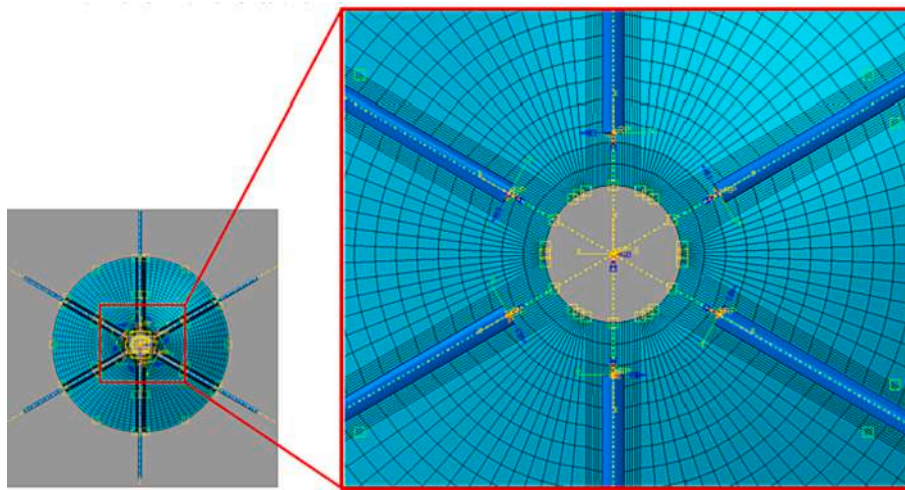
Fig. 7. Finite element model of the parabolic reflector.

Table 3
Control of element quality.

Items	Number	Average value	Worst Value
Element number	7920	—	—
Minimum Angle of quadrilateral element < 10°	0 (0 %)	82.94	67.60
Maximum Angle of quadrilateral element > 160°	0 (0 %)	97.16	114.07
Ratio of length and width > 10	0 (0 %)	3.32	9.77
Geometry eccentricity factor > 0.2	0 (0 %)	0.00160	0.0171
Minimum edge length < 0.01	0 (0 %)	2.29	0.431

Table 4
Simulation steps and boundary conditions.

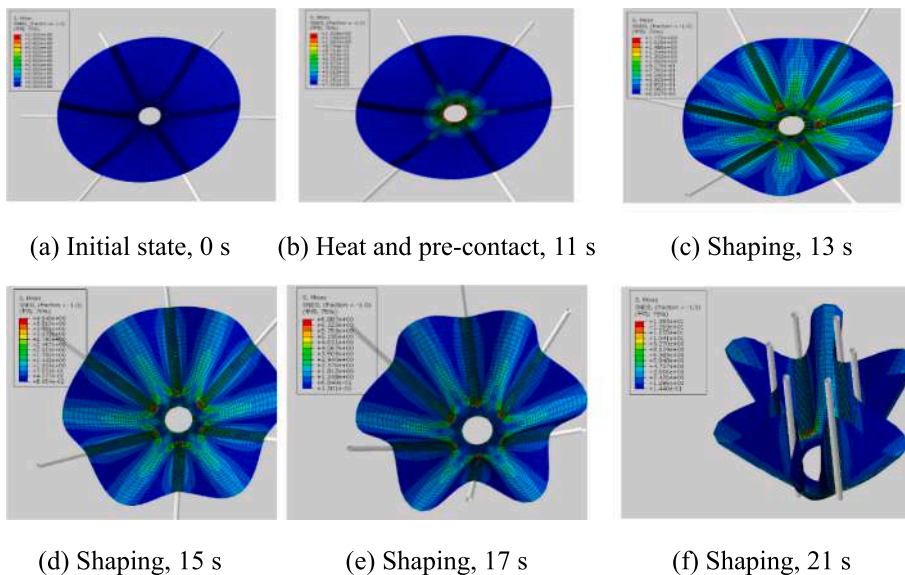|	Step	Time	Temperature field	Boundary condition
1.	Heat and pre-contact	11 s	Heat up from 30 °C to 120 °C.	Fix the reflector's reference point at its center; rotate six bars at a small angle (−0.1 rad) to establish tender contact with the reflector surface.
2.	Shaping under external force	10 s	Maintain at 120 °C.	Keep the reflector's center fixed. Rotate the six bars −1.57 rad around their own reference points located at one end of the cylinder axis to a perpendicular position.
3.	Keep fixed and cool down	180 s	Cool down to 30 °C.	Keep the reference point fixed. Keep the six bars in the perpendicular position.
4.	Unload constraints	10 s	Maintain at 30 °C.	Keep the reference point fixed. Rotate the six bars to their initial position.
5.	Heat to recover	200 s	Heat up from 30 °C to 120 °C within 100 s, and then maintain at 120 °C.	Keep the reference point fixed. Keep six bars in their initial position.

(a) Initial state, 0 s   (b) Heat and pre-contact, 11 s   (c) Shaping, 13 s

(d) Shaping, 15 s   (e) Shaping, 17 s   (f) Shaping, 21 s

Fig. 8. Process of folding using six bars to shape the reflector to its folded state.

    (g) Cool down, 0 s   (h) Cool down, 180 s   (i) Unload constraints, 190 s
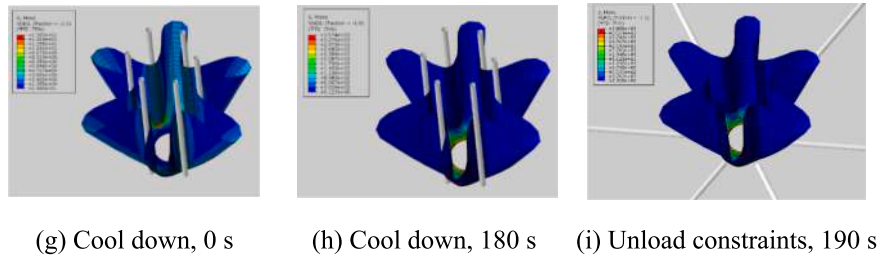
Fig. 9. Process of cooling down to memorize the folded shape and unloading constraints.

    (j) 0 s   (k) 80 s   (l) 83 s

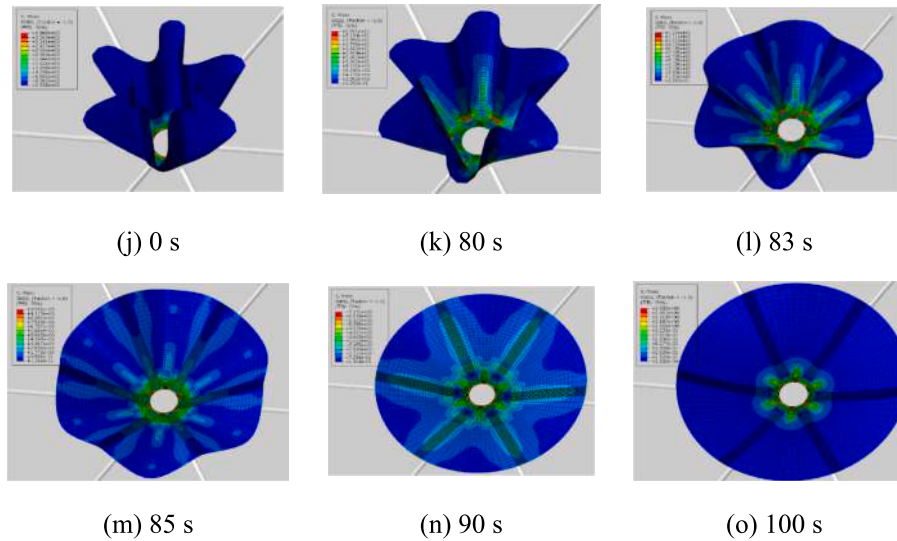   (m) 85 s   (n) 90 s   (o) 100 s

Fig. 10. Deploying process (shape recovery).

respectively.

The reflector takes 180 s to cool down from 120 °C to 30 °C to memorize its folded shape with an increasing stress value, as shown in Fig. 9 (g) to (h). The stress concentration at the reflector surface's fixed area clearly, increases from 13.83 MPa to 3570 MPa. It takes 10 s to rotate the bars to their initial position to unload the constraints, as shown in Fig. 9 (h) to (i).

As shown in Fig. 10, when the temperature field rises again from 30 °C to 120 °C, the reflector takes approximately 100 s to recover from its folded state to its initial state and it moves at a recovery speed of about 0.9° per second. Figures present the recovery state at 0 s, 80 s, 83

s, 85 s, 90 s, and 100 s respectively. The temperature at 80 s (Fig. 10 (k)) is 102 °C, higher than the glass transition temperature ($T_g = 100$ °C). As a result, the reflector begins to deploy while the overall stress level rapidly releases. The maximum stress is 23.91 MPa at the reflector's bottom. When observing the picture of the change from 80 s to 85 s (Fig. 10 (k) to (m)), the reflector quickly recovers, and the stress value decreases from 23.91 MPa to 9.996 MPa. After 85 s, the stress value reaches a low level and the reflector's recovery rate decreases. At 90 s (Fig. 10 (n)), the reflector basically recovers to its initial shape. However the stress in the contact area is higher than in the other parts as it is not fully released. At 100 s (Fig. 10 (o)), the reflector's stress is almost
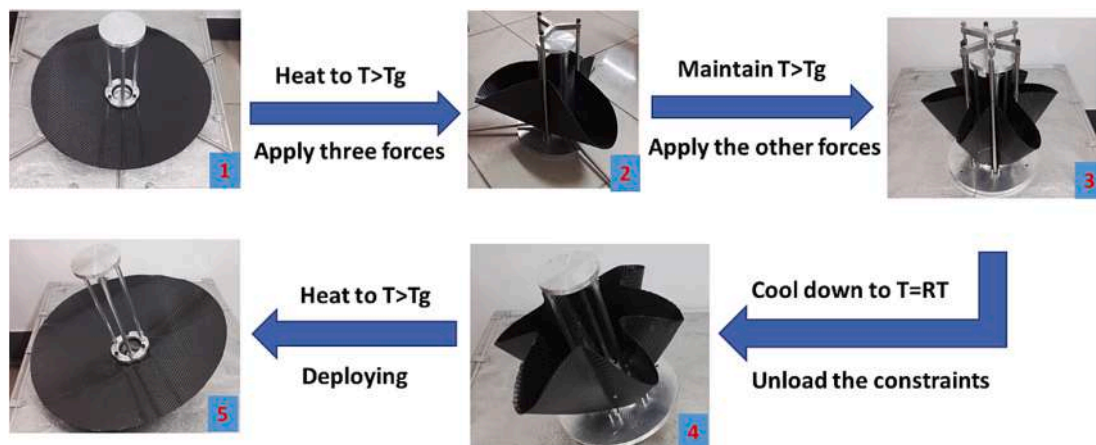

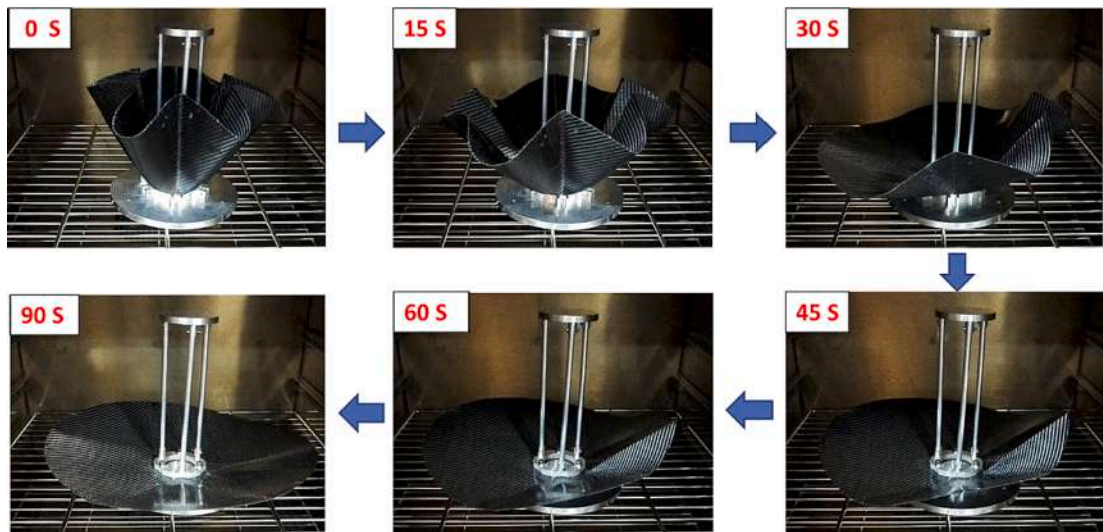**Fig. 11.** Process of the folding and deploying tests.

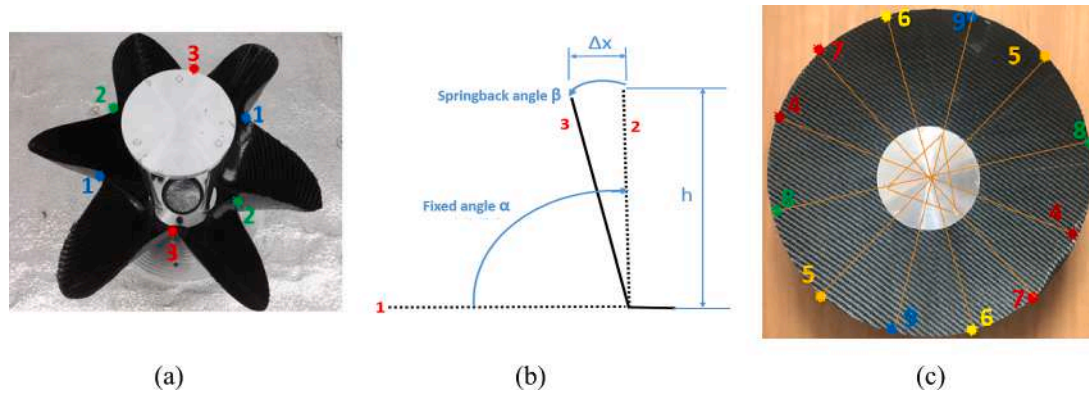**Fig. 12.** Deploying sequences in the oven.

Fig. 13. (a) Measuring points of shape fixation ratio; (b) Diagram of angle related to the reflector's shape spring; (c) Measuring points of shape recovery ratio marked on the reflector.

completely released. Only the fixed part at the reflector's bottom has stress (1.583 MPa), which may be caused by thermal stress and boundary constraints.

5. Testing

5.1. Folding and deploying tests

As shown in Fig. 11, folding and deploying tests were conducted by four steps:

1) After assembling the deployable reflector, including the six bars used to fold it, place it into an oven heated to $T > T_g$ ($T = 120\,^\circ C$ was set in the testing) for 15 min, take it out and rotate any three bars 120° apart to fold it into a three-petal configuration, and then use the top fixing tool to keep the three bars fixed in a perpendicular position.
2) Put the three-petal reflector into the oven at $120\,^\circ C$ for 15 min, take out and rotate the remaining three bars to shape the three-petal reflector into a six-petal configuration, and then use the same method to keep the last three bars fixed in a perpendicular position.
3) Cool the reflector naturally down to $T = RT$ (Room temperature, about $30\,^\circ C$), after which the six bars can be disassembled to unload the constraints. The folded shape can be fixed using the SMP itself without external force.
4) When putting the folded reflector into an oven at a temperature of above T_g, the reflector will slowly deploy to its original parabolic

shape. In addition, $T = 120\,^\circ C$ was set during the initial moment of the deploying test.

Fig. 12 shows the sequences of the deploying process. The folded reflector was placed into an oven heated to $T = 120\,^\circ C$ (Initial deploying temperature). The reflector took about 90 s to deploy. Theoretically speaking, the reflector with quasi-isotropic lamination would unfold uniformly in a constant temperature field. However, it was found that in the sequences of 30 s, 45 s, and 60 s, the deploying rate of the reflector's lower right corner is slower than other parts. During the actual test, the temperature field is not uniform and constant because the oven door was opened to film the unfolding process. The same phenomenon was observed with several folding-deploying cycles. This problem may be improved using consistent heating elements when it is used in practical engineering applications.

5.2. Shape fixation ratio and recovery ratio tests

5.2.1. Shape fixation ratio

A noticeable springback will occur after the constraints are withdrawn (occurring from Image 3 to Image 4 in Fig. 11) because the elastic strain yielded during the folding stage is released. The angle deformation before and after unloading constraints can be applied to characterize the reflector's shape fixation ratio. As shown in Fig. 13 (a), three pairs of measuring points marked with different numbers and colors were used to measure deformation. The small variation distance $(2\Delta x)$

Table 5

Shape fixation ratio.

Parameters	Points 1-1	Points 2-2	Points 3-3
Distance under constraints (mm)	91	89	89
Distance without constraints (mm)	111	116	113
Angle Changes(°)	3.576	4.822	4.289
Shape fixation ratio	96.03 %	94.64 %	95.23 %
Average shape fixation ratio		95.30 %	

Table 6

Shape recovery ratio.

Measure point	Distance (mm)	Shape recovery ratio	Average shape recovery ratio
Points 4-4	397	99.24 %	99.37 %
Points 5-5	401	99.75 %	
Points 6-6	403	99.26 %	
Points 7-7	403	99.26 %	
Points 8-8	397	99.24 %	
Points 9-9	398	99.50 %	

between the same pair of points can be measured. In Fig. 13 (b), the height of the single petal h $= 160mm$ and fixed angle α $= 90°$ are known. Therefore, Eq. (1) can be applied to calculate the springback angle β, and Eq. (2) can be applied to calculate the shape fixation ratio.

$$\beta = arctan\left(\frac{\Delta x}{h}\right) \tag{1}$$

$$\Phi_F = 1 - \frac{\beta}{\alpha} = 1 - \frac{arctan\left(\frac{\Delta x}{h}\right)}{90°} \tag{2}$$

where Φ_F is the reflector's shape fixation ratio, α is the fixed angle, β is the springback angle, Δx stands for the reflector edge's small displacement, and h stands for each petal's length.

Table 5 records the distance between two points in the same pairs. The springback angles and shape fixation ratios were calculated by applying the method mentioned above. The changes in angles are very small ($<5°$) and the fixation ratio's average value is 95.30 %, both showing that the reflector has a high capacity for shape fixation. We can find springback in experiment is bigger than that in simulation. It is due to the temperature reduction in parts of the materials which are "frozen" before completing the folding process. "Frozen" in advance will make the materials to store more elastic energy which will be released when removing external constraints. Springback can be reduced by folding the structure in a constant temperature oven, but it is impractical for large structures. In this work, the springback value is about 5 %, which is acceptable.

5.2.2. Shape recovery ratio

The variation distance of points labeled in Fig. 13 (c) is a simple way to characterize shape recovery ratio. This ratio can be calculated using Eq.(3), where the initial aperture is 400 mm, so the deployed shape after folding can be measured. Six pairs of distances were measured and listed in Table 6. The average shape recovery ratio is 99.37 %, showing a precious recovery rate of the reflector's roundness.

$$\Phi_R = \frac{\Phi_D}{\Phi_0} \tag{3}$$

where Φ_R represents the reflector's recovery ratio, Φ_D is the aperture of deployed reflector after folding, and Φ_0 is the reflector's initial aperture.

6. Conclusions

In this study, a lab-scale deployable parabolic reflector based on SMP composites was designed and fabricated. Combined with FEA, the optimal six-petal folding pattern was determined. The mechanical states and energy changes of shape memory behavior during the deformation process as well as the deploying time were obtained. In addition, the performance of the deployable reflector was evaluated by experimental tests. The experimental results demonstrated the feasibility and applicability of the designed pattern and analysis method. In accordance with the simulation results, the deployable parabolic reflector can be successfully folded and shaped with the procedure settings of temperature and external force, and can be heated to deploy successfully without any damage or failure. Obtained results from simulation and testing have a promising storage ratio, deploying reliability, shape fixation ratio, and shape recovery ratio. This effort will provide useful experience and data for further study of large deployable reflectors.

Declaration of Competing Interest

The authors declare that they have no known competing financial interests or personal relationships that could have appeared to influence the work reported in this paper.

Data availability

Data will be made available on request.

Appendix A. Supplementary material

Supplementary data to this article can be found online at https://doi.org/10.1016/j.compstruct.2022.116327.

References

[1] Mu T, Liu L, Lan X, Liu Y, Leng J. Shape memory polymers for composites. Compos Sci Technol 2018;160:169–98.

[2] Liu YJ, Du HY, Liu LW, Leng JS. Shape memory polymers and their composites in aerospace applications: a review. Smart Mater Struct 2014;23:23001–22.

[3] Leng J, Lan X, Liu Y, Du S. Shape-memory polymers and their composites: Stimulus methods and applications. Prog Mater Sci 2011;56:1077–135.

[4] Santo L, Quadrini F. Shape Memory Materials from Epoxy Matrix Composites. In: Ponnamma D, Sadasivuni KK, Cabibihan JJ, AlMaadeed MA, editors. Smart Polymer Nanocomposites: Energy Harvesting, Self-Healing and Shape Memory Applications; 2017.

[5] Roh JH, Bae JS. Softenable composite boom for reconfigurable and self-deployable structures. Mech Adv Mater Struct 2017;24:698–711.

[6] Santo L, Quadrini F, Bellisario D. Shape memory composite antennas for space applications. In: Maropoulos S, Kyratsis P, Kakoulis K, Taousanidis N, Oancea G, Dodun O, editors. 20th Innovative Manufacturing Engineering and Energy Conference; 2016.

[7] Sokolowski W, Tan S, Willis P, Pryor M. Shape memory self-deployable structures for solar sails. In: Voelcker NH, Thissen HW, editors. Smart Materials V; 2008.

[8] Wang XH, Zhang W, Lan X, Liu YJ, Leng JS. Basic properties and application of shape memory polymer composite to deployable hinge for solar arrays. In: Du S, Leng J, Asundi AK, editors. International Conference on Smart Materials and Nanotechnology in Engineering, Pts 1-3; 2007.

[9] Wei H, Liu L, Zhang Z, Du H, Liu Y, Leng J. Design and analysis of smart release devices based on shape memory polymer composites. Compos Struct 2015;133:642–51.

[10] Doel P, Kendrew S, Brooks D, Dorn C, Yates C, Martin RD, et al. Development of an active carbon fiber composite mirror. Free-Space Laser Communication and Atmospheric Propagation Xxvi. 2004:1526-33.

[11] Kendrew S, Doel P. Development of a carbon fiber composite active mirror: design and testing. Opt Eng 2005;45:535–45.

[12] Varlese SJ, Ulmer MP, Hardaway LR, Everhart M, Vaynman S, Emerson G, et al. Laminated electroformed shape memory composite for deployable lightweight optics. Earth Observing Systems IX; 2004:375-83.

[13] Thompson SJ, Doel AP, Brooks D, Strangwood M. Towards a large, lightweight mirror for AO - Development of a 1 m Ni coated CFRP mirror. Advanced Optical and Mechanical Technologies in Telescopes and Instrumentation, Pts 1-3; 2008; 7018.

[14] Zhang D, Li W, Lv Q, Liu Y, Chen X. Lightweight Design and Finite Element Analysis of Primary Mirror For The Space Telescope. In: Mazuray L, Wartmann R, Wood AP, editors. Optical Systems Design 2015: Optical Design and Engineering Vi; 2015.

[15] Lin W-C, Chang S-T, Yu Z-R, Lin Y-C, Ho C-F, Huang T-M, et al. Comparing optical test methods for a lightweight primary mirror of a space-borne Cassegrain telescope. Meas Sci Technol 2014;25.

[16] Chen PC, Bowers CW, Content DA, Marzouk M, Romeo RC. Advances in very lightweight composite mirror technology. Opt Eng 2000;39:2320–9.

[17] Chen PC, Saha TT, Smith AM, Romeo R. Progress in very lightweight optics using graphite fiber composite materials. Opt Eng 1998;37:666–76.

[18] Abusafieh AA, Connell SJ, Cohen EJ. Dimensional stability of CFRP composites for space-based reflectors. Proc SPIE - Int Soc Opt Eng 2001;4444:9–16.

[19] Zhong P, Li C, Jing N, Chong Y, Ren G. Research on Lightweight Passive Deployment Mechanism for the Secondary Mirror in the Deployable Space Telescope. In: Luo X, Ye T, Xin T, Hu S, Hong M, Gu M, editors. 8th International Symposium on Advanced Optical Manufacturing and Testing Technologies: Design, Manufacturing, and Testing of Micro- and Nano-Optical Devices and Systems; and Smart Structures and Materials; 2016.

[20] Barber GJ, Braem A, Brook NH, Cameron W, D'Ambrosio C, Harnew N, et al. Development of lightweight carbon-fiber mirrors for the RICH 1 detector of LHCb. Nucl Instrum Methods Phys Res Section a-Accelerators Spectrometers Detectors Associated Equipment 2008;593:620–33.

[21] Arzberger SC, Munshi NA, Lake MS, Wintergerst J, Varlese S, Ulmer MP. Elastic memory composite technology for thin, lightweight space and ground-based deployable mirrors. In: Goodman WA, editor. Optical Materials and Structures Technologies; 2003: 143-54.

[22] Barrett R, Taylor R, Keller P, Codell D, Adams L. Deployable Reflectors for Small Satellites; 2007.

[23] Deployable Tensegrity Reflectors for Small Satellites; 2008.

[24] Thompson SJ, Doel P, Brooks D, Strangwood M. A 1-metre Ni coated CFRP demonstrator for large deformable mirrors. 1st AO4ELT conference - Adaptive Optics for Extremely Large Telescopes; 2010.

[25] Lightsey PA. James Webb Space Telescope: large deployable cryogenic telescope in space. Opt Eng 2012;51:011003.

[26] Keller P, Lake M, Codell D, Barrett R, Taylor R, Schultz M. Development of Elastic Memory Composite Stiffeners for a Flexible Precision Reflector. Aiaa/asme/asce/ahs/asc Structures, Structural Dynamics, and Materials Conference Aiaa/asme/ahs Adaptive Structures Conference; 2006:1-14.

[27] Muller J. Antenna Theory Analysis And Design; 2016.

[28] Jape S, Garza MR, Ruff J, Espinal FA, Sessions D, Huff G, et al. Self-foldable origami reflector antenna enabled by shape memory polymer actuation. Smart Mater Struct 2020;29:115011.

[29] Hernandez EAP, Hartl DJ, Lagoudas DC, Asme. ANALYSIS AND DESIGN OF AN ACTIVE SELF-FOLDING ANTENNA. Proceedings of the Asme International Design Engineering Technical Conferences and Computers and Information in Engineering Conference, 2017; 58189 : V05BT08A049.

[30] Zeng H, Leng J, Gu J, Sun H. A thermoviscoelastic model incorporated with uncoupled structural and stress relaxation mechanisms for amorphous shape memory polymers. Mech Mater 2018;124:18–25.

[31] Nguyen TD, Qi HJ, Castro F, Long KN. A thermoviscoelastic model for amorphous shape memory polymers: Incorporating structural and stress relaxation. J Mech Phys Solids 2008;56:2792–814.

[32] Williams ML, Landel RF, Ferry JD. The temperature dependence of relaxation mechanisms in amorphous polymers and other glass-forming liquids. J Am Chem Soc 1955;77:3701–7.

[33] Xiao H, Chen L. Hencky's elasticity model and linear stress-strain relations in isotropic finite hyperelasticity. Acta Mech 2002;157:51–60.

[34] Chen J, Liu L, Liu Y, Leng J. Thermoviscoelastic shape memory behavior for epoxy-shape memory polymer. Smart Mater Struct 2014;23:055025.